Journal Pre-proof

The structural, electrical and optical properties of spark plasma sintered $BaSn_{1-x}Sb_xO_3$ ceramics

Jelena Vukašinović, Milica Počuča-Nešić, Danijela Luković Golić, Vesna Ribić, Zorica Branković, Slavica M. Savić, Aleksandra Dapčević, Slavko Bernik, Matejka Podlogar, Matej Kocen, Željko Rapljenović, Tomislav Ivek, Vladimir Lazović, Biljana Dojčinović, Goran Branković

PII: S0955-2219(20)30532-X

DOI: https://doi.org/10.1016/j.jeurceramsoc.2020.06.062

Reference: JECS 13389

To appear in: *Journal of the European Ceramic Society*

Received Date: 4 February 2020

Revised Date: 21 June 2020

Accepted Date: 23 June 2020

Please cite this article as: Vukašinović J, Počuča-Nešić M, Golić DL, Ribić V, Branković Z, Savić SM, Dapčević A, Bernik S, Podlogar M, Kocen M, Rapljenović Ž, Ivek T, Lazović V, Dojčinović B, Branković G, The structural, electrical and optical properties of spark plasma sintered $BaSn_{1-x}Sb_xO_3$ ceramics, *Journal of the European Ceramic Society* (2020), doi: https://doi.org/10.1016/j.jeurceramsoc.2020.06.062

This is a PDF file of an article that has undergone enhancements after acceptance, such as the addition of a cover page and metadata, and formatting for readability, but it is not yet the definitive version of record. This version will undergo additional copyediting, typesetting and review before it is published in its final form, but we are providing this version to give early visibility of the article. Please note that, during the production process, errors may be discovered which could affect the content, and all legal disclaimers that apply to the journal pertain.

© 2020 Published by Elsevier.

Journal Pre-proof

The structural, electrical and optical properties of spark plasma sintered $BaSn_{1-x}Sb_xO_3$ ceramics

Jelena Vukašinović[1*], Milica Počuča-Nešić[1], Danijela Luković Golić[1], Vesna Ribić[1], Zorica Branković[1], Slavica M. Savić[2], Aleksandra Dapčević[3], Slavko Bernik[4], Matejka Podlogar[4], Matej Kocen[4], Željko Rapljenović[5], Tomislav Ivek[5], Vladimir Lazović[6], Biljana Dojčinović[7], Goran Branković[1]

[1]Institute for Multidisciplinary Research, University of Belgrade, Kneza Višeslava 1a, 11030 Belgrade, Serbia

[2]BioSense Institute, University of Novi Sad, Zorana Đinđića 1, 21000 Novi Sad, Serbia

[3]Faculty of Technology and Metallurgy, University of Belgrade, Karnegijeva 4, 11120 Belgrade, Serbia

[4]Jožef Stefan Institute, Department for Nanostructured Materials, Jamova cesta 39, 1000 Ljubljana, Slovenia

[5]Institute of Physics, Bijenička cesta 46, HR-10001 Zagreb, Croatia

[6]Institute of Physics, University of Belgrade, Pregrevica 118, 11080 Belgrade, Serbia

[7]Institute of Chemistry, Technology and Metallurgy, Njegoševa 12, 11000 Belgrade, Serbia

*Corresponding author:

e-mail: jelena.vukasinovic@imsi.bg.ac.rs

Tel.: +381 11 2085032; Fax: +381 11 2085 038

Highlights

- Low Angle Grain Boundaries (LAGBs) present in Spark plasma sintered Sb-doped $BaSnO_3$.
- Loss of potential barrier at LAGBs drastically decreased electrical resistivity.
- Doping of $BaSnO_3$ with Sb led to linearization of *I-U* characteristic.
- $BaSn_{0.92}Sb_{0.08}O_3$ can be used as linear resistor even at higher temperatures.

Abstract

Journal Pre-proof

Antimony doped barium-stannate dense ceramic materials were synthesized using spark plasma sintering technique out of mechanically activated precursor powders. The influence of various Sb concentrations (x = 0.00 – 0.10) on properties of $BaSn_{1-x}Sb_xO_3$ ceramics was investigated. Relative densities of prepared samples were in the range of (79 – 96) %. TEM analysis revealed the presence of many dislocations in undoped $BaSnO_3$, and their significant reduction upon doping with Sb. All samples except $BaSn_{0.92}Sb_{0.08}O_3$ exhibit non-linear *I-U* characteristic, typical for semiconductors with potential barrier at grain boundaries. Low angle grain boundaries found only in $BaSn_{0.92}Sb_{0.08}O_3$ caused the loss of potential barrier at grain boundaries which was confirmed by AC impedance spectroscopy measurements. Consequently, $BaSn_{0.92}Sb_{0.08}O_3$ showed the lowest electrical resistivity and linear *I-U* characteristic. UV-Vis analysis confirmed the increasing of band gap (Burstein–Moss shift) values in all doped samples.

Keywords: $BaSnO_3$; Spark plasma sintering; Potential barrier; Low angle grain boundaries; Electrical conductivity

1. Introduction

In polycrystalline metal oxide ceramic materials common intrinsic defects are oxygen vacancies making these materials n-type semiconductors, while the grain boundary interfaces are p-type due to existence of trapping states. As a result, the potential barrier is formed at grain boundary, influencing the charge carrier transport and dominating the electrical properties of such semiconductor. In order to obtain highly conductive metal oxide ceramic material with linear *I-U* characteristic in a wide voltage range, the formation of potential barrier should be avoided [1].

Journal Pre-proof

Journal Pre-proof

The electroceramic materials with perovskite structure (AMO_3) exhibit diverse physical properties such as superconductivity, colossal magnetoresistance, ferroelectricity, ferromagnetism and piezoelectricity [2, 3]. These properties offer many possible applications of perovskite materials in the fabrication of resistors, electrodes, components of heating devices [4], perovskite solar cells, photocatalysts or gas sensors [5 – 7].

Barium stannate, $BaSnO_3$ (BSO), belongs to the perovskite-type alkaline earth stannates, $ASnO_3$ (A = Ca, Sr, Ba) [5, 6 – 9] and it crystallizes in an ideal cubic perovskite structure (space group: $Pm\bar{3}m$). The larger Ba^{2+} cations coordinated with twelve O^{2-} anions form a cubic close-packed lattice, while smaller Sn^{4+} cations occupy octahedral holes formed by oxygen anions. As a result, the crystal structure of BSO consists of a 3D network of corner-sharing [SnO_6] octahedra with Ba^{2+} ions occupying the 12-fold coordination site formed in the middle of the cube of eight such octahedra [10 – 12]. Chemical and thermal stability at temperatures up to 1000 °C, optical transparency in the visible region [7, 13, 14], simple fabrication and non-toxicity make BSO suitable for many applications: as a photocatalyst, photoanode material for dye-sensitized solar cells [5, 13 – 16], dielectric capacitor [5, 6, 9, 15, 16], proton conductor [12,13], protective coating or catalyst support [5], gas sensor [5 – 7, 9, 13, 15 – 19] etc. Its high electron mobility enables the use of $BaSnO_3$ in electronics, especially in Field-effect transistors as an active channel material [20]. For all aforementioned purposes, $BaSnO_3$ has been synthesized in the forms of ceramic materials [2, 4, 6, 8, 9, 19, 21 – 26], single crystals [20, 27, 28] and thin films [29, 30], using various synthetic approaches such as solid state reaction [2, 4, 6, 9, 19, 21 – 24, 26], flux method [20, 27, 28], pulsed laser deposition [29], chemical solution deposition (CSD) [30] and molecular beam epitaxy [31, 32].

BSO is a wide band-gap semiconductor [5, 13, 19], but appropriate doping can alter its electrical characteristics. Replacement of tin with yttrium or indium (M-site doping) changes

Journal Pre-proof

BSO into a proton conductor [33]. On the other hand, after replacement of Ba^{2+} with La^{3+} (A-site doping) or Sn^{4+} with Sb^{5+}, BSO becomes n-type semiconductor with high electrical conductivity at 25 ºC [2, 4, 8, 21].

The synthesis of the single phase Sb-doped BSO raises several problems. The electrical and optical properties of BSO are strongly correlated with the amount of antimony since these ions induce the formation of defects and local distortions within the BSO crystal lattice. According to the literature, the maximum solubility of Sb in BSO can reach 20 mol % [2, 4, 22, 23], whereas for the single crystals, the doping level is 10 mol% [27]. It is known that Sb ions can be segregated at the particle surface, forming Sb-rich secondary phase and inhibiting the grain growth [34]. High Sb concentration present in the system can also result in the formation of $BaSb_2O_6$ and SnO as secondary phases, thus affecting the phase composition [4, 24, 27]. Another problem, which hinders the preparation of single phase BSO-based ceramics, is the formation of the tetragonal phase Ba_2SnO_4, with large band gap and high electrical resistivity [25, 35].

The major drawback of BSO-based ceramics is its low density [6, 9]. The conventional solid state procedure requires long thermal treatments with several intermittent grinding and heating steps at temperatures up to 1600 °C [6, 9]. Still, these conditions cannot sufficiently enhance the densification process of the ceramic material, even with the use of sintering aids like polyvinyl alcohol or SiO_2 [4, 6, 9, 25]. In order to overcome these problems, an alternative sintering method should be used. The spark plasma sintering (SPS) technique, which includes simultaneous application of high pressure and heat during a short period of time, is known as an efficient method for the preparation of dense ceramic samples. SPS lowers the sintering temperature and shortens the overall processing time in comparison with the conventional sintering process [36]. It was successfully used in the preparation of various perovskite ceramic materials like $BiFeO_3$, $BaTiO_3$, $SrTiO_3$ [36 – 38] including La-doped

Journal Pre-proof

$BaSnO_3$ [8], but, to the best of our knowledge, there are no literature reports about its use for the Sb-doped $BaSnO_3$.

The attention has been previously focused on the structural, electrical or optical properties of $BaSnO_3$-based ceramics, but with the lack of information about the microstructural properties, especially for the Sb-doped $BaSnO_3$ [2, 4, 8, 14, 16, 21 – 23]. The aim of this work was to prepare $BaSn_{1-x}Sb_xO_3$ ceramics with linear *I-U* characteristic, large electrical conductivity and higher density. The precursor powders obtained from mechanically activated $BaCO_3$, SnO_2 and Sb_2O_3 were sintered using SPS technique. In this process, the low melting point of Sb_2O_3 (656 °C) [6] enabled sintering in the liquid phase, thus providing better contact between particles and improving material transport within the liquid phase. Structural, microstructural, electrical and optical characterizations of $BaSn_{1-x}Sb_xO_3$ ceramic samples were performed. For the first time, *I-U* characteristics of the obtained ceramics were observed at temperatures above 25 °C and the electrical conductivity of $BaSn_{1-x}Sb_xO_3$ ceramics was investigated. The correlation between structural, microstructural and electrical properties was established.

2. Materials and methods

The precursor powders of $BaSn_{1-x}Sb_xO_3$, (x = 0.00, 0.04, 0.06, 0.08, and 0.10) were prepared by mechanical activation using $BaCO_3$ (99.95 %, Alfa Aesar), SnO_2 (99.9 %, Alfa Aesar) and Sb_2O_3 (99 %, Merck) powders as starting reagents. The starting powders, weighed in appropriate stoichiometric ratios, were activated in a planetary ball mill (Fritsch Pulverisette 5) using isopropanol as the medium. The mixture of starting powders and tungsten carbide (WC) balls were placed in a WC cylindrical vial, with the 25:1 ball-to-powder weight ratio. The milling time was 8 h, and the rotational speed of disc was 120 rpm. Dried powders were calcined at 900 °C for 4 h in air.

Journal Pre-proof

Sintering was performed in a SPS furnace (FAST, Dr. Sinter FAST 515-S, Sumimoto FAST Syntex Ltd., Japan) under vacuum conditions using a graphite die with the diameter of 10 mm. The calcined powders were heated with the heating rate of 100 °C/min and sintered at 1200 °C for 5 minutes. Uniaxial pressure of 60 MPa was applied before the heating process and maintained until the sample was cooled to room temperature. For the characterization of ceramic materials thin slices of the sintered samples were cut from the both parallel sides. Afterwards, the surfaces were polished by sandpaper and annealed at 700 °C for 2 h in air in order to remove the surface carbon contamination and compensate the oxygen deficiency formed during sintering in reduction atmosphere [36, 37].

The X-ray powder diffraction (XRD) analysis was determined on Rigaku Ultima IV, Japan, with CuKα radiation (λ = 0.154 nm) from 20 ° to 90 ° (2θ) with a step-width of 0.02 ° and scanning rate of 0.2 °/min. *PowderCell* (version 2.4) software was used for the phase composition and crystallite size analysis. The unit cell parameters were calculated by the least squares methods using the *LSUCRI* software [39]. The contents of Ba, Sb and Sn were determined by inductively coupled plasma optical emission spectrometry (ICP-OES). ICP-OES measurement was performed using Thermo Scientific iCAP 6500 Duo ICP (Thermo Fisher Scientific, Cambridge, United Kingdom). The digestion of samples was performed on Advanced Microwave Digestion System (ETHOS 1, Milestone, Italy) using HPR-1000/10S high pressure segmented rotor at temperature of 160 ºC for 15 minutes. The microstructure was investigated by the Field Emission Scanning Electron Microscope (FESEM, MIRA3 FEG-SEM, Tescan), Scanning Electron Microscope (SEM, TESCAN Vega TS5130MM) equipped with the Energy dispersive spectroscopy (EDS, Oxford Instruments, model INCA PentaFETx3). FESEM analysis was examined on fractured cross-sections of sintered samples, while SEM and EDS analyses were performed on the polished cross-section of the pure sintered sample after thermal etching at 1100 °C for 20 minutes in the air atmosphere.

Journal Pre-proof

The average grain size was measured as the mean linear intercept method using the ImageJ software. For the Transmission Electron Microscopy (TEM) analysis pellets were cut into 3 mm discs using an ultrasonic cutter (SONICUT380, SBT, USA) and further mechanically thinned to 100 μm. The discs were then dimpled down to 20 μm in the center (Dimple grinder 656, Gatan Inc., USA), and finally ion-milled (PIPS 691, Gatan Inc., USA) using 4 kV Ar^+ ions at an incidence angle of 8 ° to obtain large transmissive areas for the TEM investigations. TEM, High Resolution Transmission Electron Microscopy (HRTEM) and Selected Area Electron Diffraction (SAED) analyses were performed using a 200 kV ultra-high-resolution field-emission gun (FEG) transmission electron microscope (JEM 2010F, Jeol, Japan).

The DC electrical conductivity of samples coated with Au electrodes was measured using Keithley 237 High Voltage Source Measure Unit. These measurements were performed in air in the temperature range of (25 – 150) °C, with the step of 25 °C.

The AC impedance spectroscopy measurements were performed in the frequency range of 5 kHz – 5 MHz on the HIOKI 3532-50 impedance analyzer at 25 ºC in air. EIS Spectrum Analyzer software was used for the fitting of experimental data collected for samples with x = 0.00 and 0.04.

Hall effect measurements were performed at 290 K, in magnetic fields -5 T to 5 T perpendicular to the current through the sample. Samples were cut for the Hall-bar geometry with typical dimensions 10 mm × 2 mm × 1 mm. Two current contacts and three pairs of Hall contacts were made by applying DuPont 4929N silver paint. Hall signal was antisymmetrized, $V_{yx} = [V_{yx}(+B) - V_{yx}(-B)]/2$, in order to eliminate the possible mixing of the magnetoresistance component. Hall resistance, $R_{yx} = V_{yx}/I$, was found to be linear with magnetic field B for all samples and the Hall coefficient was obtained as $R_H = V_{yx}\, t/(IB)$, where I is the current and t the sample thickness.

Journal Pre-proof

Ultraviolet-Visible diffuse reflectance spectra (UV-Vis DRS) of pulverized pellets were measured using Shimadzu UV-2600 Spectrophotometer.

3. Results and discussion

3.1. XRD and ICP-OES analyses

According to the XRD patterns, all calcined $BaSn_{1-x}Sb_xO_3$ powders consist of cubic $BaSnO_3$ (space group: $Pm\bar{3}m$, PDF # 89-2488), with the presence of small amounts of unreacted SnO_2 (space group: $P4_2/mnm$, PDF # 88–0287) and $BaCO_3$ (space group: $Pmcn$, PDF # 71-2394) (Figure 1).

Fig.1.

After the sintering process, small soft silvery gray beads were observed on the top of the graphite die. ICP-OES analysis revealed that these are mainly composed of tin with traces of antimony and barium. Resulted molar ratio Sn : Ba : Sb in the beads (for the sample $BaSn_{0.96}Sb_{0.04}$) was 5.6 : 0.6 : 0.03. The presence of these elements was also confirmed by BS-SEM and EDS analyses (see Supplementary material). During the SPS process the reaction between graphite die and oxygen from the sample can occur at temperatures lower than 600 °C [36], leading to the formation of CO phase. Vacuum atmosphere, high pressure and non-uniform temperature distribution from the center to the edge of sample together with created reduction atmosphere can cause the reduction of metal ion even to elementary state, *i.e.* Sn^{4+} can be reduced to Sn^{2+} or metallic Sn [40 – 43]. We can assume that Ba, Sn and Sb – cations in our samples are partially reduced to their elementary state. The low melting temperatures (T_m (Sn) = 232 °C, T_m (Sb) = 631 °C, T_m (Ba) = 727 °C) [44] of these metals enable the formation of the liquid phase while the vacuum atmosphere with high uniaxial pressure induces its partial evaporation and promotes the injection of the liquid phase out of

Journal Pre-proof

the die. Since tin has the highest vapor pressure, it was expected that tin would evaporate with the highest rate.

Figure 2 shows the XRD patterns for pulverized annealed $BaSn_{1-x}Sb_xO_3$ ceramic samples after the SPS treatment. They reveal the presence of the cubic $BaSnO_3$ (space group: $Pm\bar{3}m$, PDF # 89-2488) as a dominant phase, and tetragonal Ba_2SnO_4 (space group: $I4/mmm$, PDF # 74-1349) as a secondary phase, with no reflections belonging to SnO_2 or $BaCO_3$. Upon doping, the amount of secondary phase changes from 15 wt % in undoped samples to 7–8 wt % in doped ones (Table 1). However, the reduced content of tin in BSSO samples, due to its volatilization during SPS process led to the non-stoichiometry and enabled the formation of barium-rich phase Ba_2SnO_4.

Fig. 2.

In comparison with the undoped $BaSnO_3$, all reflections of doped samples are shifted towards lower 2θ angles as a consequence of the increased unit cell parameter a (Figure 2b, Table 1). The increase of the Sb concentration led to the expansion of unit cell, as was previously reported [2, 21, 24, 26]. Having in mind that in the six-coordinated geometry, the ionic radius of Sn^{4+} (r = 0.069 nm) lies between the values of Sb^{3+} (r = 0.072 nm) and Sb^{5+} (r = 0.060 nm) ionic radii, one could assume that the unit cell expansion is a result of Sb^{3+} ions present in the crystal lattice. However, in this case it could not be explained only by consideration of ionic radii, but it should be correlated with the electronic band structure of $BaSn_{1-x}Sb_xO_3$. First-principles calculations along with the experimental data provided by Kim et al. [27] pointed out that this kind of unit cell expansion is a result of equilibrium ions' arrangement due to the achievement of the minimal Coulomb energy, because the electronic states in the antibonding conduction band of $BaSnO_3$ cause repulsive forces between Sn and O upon Sb-doping [27].

Journal Pre-proof

The values of crystallite size for $BaSn_{1-x}Sb_xO_3$ samples are in the range (37–57) nm (Table 1). The observed differences in crystallite size and unit cell parameter among doped samples are the result of lattice distortion and internal stress caused by Sb-doping.

Table 1.

Taking into account densities of the samples and the results of preliminary electrical characterization, three samples (x = 0.00, 0.04 and 0.08) were selected for ICP-OES analysis in order to determine the amount of antimony present and overall molar ratio of constituent cations. In all BSSO samples the content of Sn is significantly lower than experimentally targeted, as a result of the its volatilization during SPS treatment (Table 2). Based on presented results it is expected that volatilization of all cations, together with the presence of Ba_2SnO_4, will affect properties of obtained ceramic samples. However, ICP results indicate that ratio between Ba and Sb is almost the same as experimentally defined, suggesting that the electrical properties of doped $BaSnO_3$, should be improved upon doping despite of partial material loss due to volatilization.

Table 2.

3.2. Microscopy analyses

3.2.1. FESEM and SEM analyses

Relative densities of all $BaSn_{1-x}Sb_xO_3$ ceramic samples were in the range of (79–96) % (Table 1). FESEM micrographs of the fractured cross-sections of undoped BSO showed well-densified microstructure, but non-homogeneous grain size distribution (Figure 3a). The Sb-doped ceramics showed more homogenous microstructure than the undoped one, with the decrease of the grain size upon increasing the dopant concentration (Figure 3b-e). The average grain size of all BSO samples is presented in Table 1. Even though the grain growth

Journal Pre-proof

inhibition could be correlated with the structure defects and Sb segregation on the surface of the grains [34], the latter was not confirmed by means of electron microscopy or XRD analyses.

Fig. 3.

In order to define location, morphology and composition of secondary phase, BS-SEM and EDS analyses were performed on the undoped BSO sample since it showed the highest content of the Ba_2SnO_4 phase. This phase was not detected in fractured and polished sample, but thermal etching revealed the presence of secondary phase on the surface of the sample (Figure 4). Comparing the FE-SEM and BS-SEM micrographs we could conclude, that the Ba_2SnO_4 phase was uniformly distributed through the sample's volume, and that thermal etching induced its diffusion to the sample's surface. EDS analysis of undoped BSO sample (Figure 4, Table 3, Spectra 1 and 2) showed the atomic ratio between constituent elements (Ba, Sn, and O) corresponding to the $BaSnO_3$ phase. Still there are positions on the sample's surface having higher content of Ba in comparison to tin, indicating the presence of secondary phase (Figure 4, Table 3, Spectra 3 and 4).

Fig. 4.

Table 3.

3.2.2. TEM, HRTEM and SAED analyses

Additional microstructural analyses, using TEM and HRTEM techniques, were performed on $BaSn_{1-x}Sb_xO_3$ (x = 0.00, 0.04 and 0.08) ceramic samples with densities higher than 85 %. TEM analysis of the undoped $BaSnO_3$ revealed the presence of many dislocations caused by the internal stress (dislocations are marked with white arrows on Figure 5a) and also a layer of amorphous phase (up to 2 nm thick) present in the grain boundary region. This amorphous phase is probably formed as a result of the changes in the grain orientations (Grain 1 and

Journal Pre-proof

Grain 2) and the formation of the high angle grain boundary (HAGB) between these differently oriented grains. HRTEM micrograph of the same sample, shows two grains, Grain 1 is oriented along [100] direction with visible (010) and (001) lattice planes, whereas the Grain 2 is not exactly, but close to [110] orientation with (1-10) and (001) planes (Figure 5b). The angle between the (001) planes of Grain 1 and Grain 2 is roughly 27°which makes the interface a high-angle tilt boundary. The interplanar distance of 0.292 nm, measured from the same HRTEM micrograph (Grain 2, Figure 5b) corresponds to the (1-10) crystal planes of BSO according to PDF card # 89-2488.

Fig. 5.

Sb-doping of BSO resulted in a more ordered microstructure with higher crystallinity. Also, the significant reduction of the grain size and the concentration of dislocations were observed in the $BaSn_{0.96}Sb_{0.04}O_3$ sample (Figure 6a). HRTEM micrograph of $BaSn_{0.96}Sb_{0.04}O_3$ sample showed Grain 1 oriented along [001] direction (Grain 1, Figure 6b) with diffractions from (200) and (110) crystal planes, and the Grain 2 with the only calculated *d*-spacing of 0.239 nm, corresponding to the (111) crystal planes of cubic BSO (space group $Pm\bar{3}m$). Considering the facts that (111) crystal plane of the Grain 2 is almost parallel to the (200) crystal plane of the Grain 1 (Figure 6b), and that angle between these planes in space group $Pm\bar{3}m$ is 54.74 º, we can conclude that the angle between these two grains is close to 54 º, forming the HAGB.

Fig. 6.

Figure 7 presents TEM micrograph of $BaSn_{0.92}Sb_{0.08}O_3$sample which revealed well-crystallized structure with the crystallite size in the range of (47–300) nm. All diffractions corresponding to cubic BSO phase were detected on the SAED pattern (Figure 7, Inset) and the most intense reflection (110) of cubic BSO appeared at *d*-spacing of 0.293 nm. Other,

Journal Pre-proof

weaker diffraction reflections (220), (211), (321), were also found and marked on SAED patterns. The overlapping of diffractions originates from the neighboring grains.

Fig. 7.

HRTEM micrograph of $BaSn_{0.92}Sb_{0.08}O_3$ ceramic sample presented in Figure 8a revealed the presence of grains with [110] and [111] orientation. It also revealed the presence of Low Angle Grain Boundaries (LAGBs) between two grains oriented along [110] direction (Grain 1 and Grain 2), with the formed angle of ~ 4.43 °. In literature, LAGBs are described as series of dislocations stacked one above the other with a low tilt formed between the grains on the opposite sides of the grain boundary [45, 46]. However, the grain boundaries existing between two grains oriented along different directions, [110] and [111] (Figure 8a), cannot be described as LAGB since the angle between them is at least 35 ° [47]. The facets of interface between two grains on Figure 8b indicate that there is some special crystallographic relationship.

The lattice fringes in Grain 2 correspond to (110) planes of cubic BSO phase with *d*-spacing of 0.293 nm. LAGBs are also formed between two grains oriented along [111] direction with angle being ~ 7.11 °.

Fig. 8.

3.3. Electrical characterization (*I-U* characteristic), AC impedance spectroscopy and Hall effect

Electrical measurements conducted on spark plasma sintered $BaSn_{1-x}Sb_xO_3$ samples confirmed the assumption that Sb-doping can improve the electrical properties of BSO.

As mentioned previously, the $BaSn_{1-x}Sb_xO_3$ (x = 0.00, 0.04 and 0.08) samples were selected for further examination.

Journal Pre-proof

The undoped $BaSnO_3$ revealed non-linear *I-U* characteristic (Figure 9, Inset) typical for semiconductors with double Schottky barrier at grain boundaries. After doping with lower concentration (x = 0.04) of Sb the electrical resistivity was decreased, but the sample retained non-linear *I-U* characteristic (Figure 9).

Fig. 9.

The change from non-linear to linear *I-U* characteristics was observed for the $BaSn_{0.92}Sb_{0.08}O_3$ sample, indicating the loss of potential barrier at grain boundaries (Figure 9). This change is primarily ascribed to the existence of LAGBs in this sample. The formed LAGBs do not possess potential barriers because of almost negligible change in the grains orientation. Owing to their low activation energy, they provide energetically more favorable path for the charge carriers' transport, having the highest impact on the electrical properties of $BaSn_{0.92}Sb_{0.08}O_3$ sample [45]. The DC electrical resistivity of all ceramic samples, measured at 25 ºC, decreased with the increase of antimony concentration and these values are presented in Table 4. The sample with x = 0.08 showed the lowest electrical resistivity of 1.09 Ωcm.

Table 4.

To the best of our knowledge, there are no literature reports about electrical characteristics of Sb-doped barium stannate at temperatures above 25 ºC. Electrical resistivity of $BaSn_{1-x}Sb_xO_3$ (x = 0.00, 0.04 and 0.08) samples observed in the temperature range of (25 – 150) °C is shown on Figure 10. It can be seen that Sb-doping also improves electrical properties of $BaSnO_3$ ceramics at higher temperatures. The introduction of Sb (x = 0.04) into $BaSnO_3$ reduced the influence of temperature on sample's electrical resistivity (Figure 10b). Furthermore, $BaSn_{0.92}Sb_{0.08}O_3$ sample showed the lowest electrical resistivity, which remained almost constant in the specified temperature range (Figures 10b and 10c).

Fig. 10.

Journal Pre-proof

In order to confirm the absence of potential barrier at grain boundaries in some of the samples, and to separate the contribution of grains and grain boundaries on the electrical properties of $BaSn_{1-x}Sb_xO_3$ samples (x = 0.00, 0.04 and 0.08; at 25 °C) the AC impedance spectroscopy was used, and the results are presented in Figure 11. The existence of one semicircle was confirmed in the case of undoped and $BaSn_{0.96}Sb_{0.04}O_3$ samples. The equivalent circuit used for fitting consisted of two resistors (R_b and R_{gb}, where "b" and "gb" denote bulk and grain boundary region) and a constant phase element (CPE) (Figure 11, Inset). The obtained results of grain and grain boundary resistivity, capacitance and coefficient of CPE are shown in the Table 5.

Fig. 11.

Table 5.

We can assume that impedance results for the samples with x = 0.00 and 0.04 originate mostly from the grain boundaries. The values of total electrical resistivity from AC impedance spectra are in agreement with the values of DC electrical resistivity obtained from *I-U* measurements (Table 4). On the other hand, the spectrum of $BaSn_{0.92}Sb_{0.08}O_3$ could not be fitted since all measured resistivity values in the applied frequency region were almost identical, and amounted about 1.12 Ωcm. This significant drop in the resistivity, noticed by DC measurements as well, originates from the loss of potential barrier at low angle grain boundaries. It manifested through the complete loss of semicircle in the impedance spectrum.

The results of Hall measurements are presented in Table 6. The negative value of the Hall coefficient at 290 K confirmed that prepared $BaSn_{1-x}Sb_xO_3$ ceramic samples show n-type conductivity indicating the replacement of Sn^{4+} with Sb^{5+} in the $BaSnO_3$ lattice. The magnitude of Hall coefficient at 290 K decreases monotonously with Sb concentration. Taking into account that oxygen vacancies intrinsically dope this system, in order to estimate charge carrier density and mobility we can assume a single n-type carrier is responsible for

Journal Pre-proof

electric transport. Its density n and mobility μ can then be obtained from room temperature bulk resistivity ρ_b, Hall coefficient R_H, and electron charge e as $n = 1 / |e\, R_H|$, $\mu = |R_H / \rho_b|$ (Table 6). In this simplified picture the decreased resistivity of polycrystalline $BaSn_{0.92}Sb_{0.08}O_3$ sample stems from increased mobility of charge carriers compared to the parent compound, but predominantly from the loss of potential barrier due to the presence of low angle grain boundaries.

The electrical resistivity of the $BaSn_{0.92}Sb_{0.08}O_3$ polycrystalline ceramic sample is still higher than achieved in the BSSO thin films [29] and single crystals [20, 27], which showed the lowest electrical resistivity of 2.43×10^{-3} Ωcm and 0.66×10^{-3} Ωcm, respectively, measured at RT. Also, the values of charge carrier density and electrical mobility of the BSSO ceramic samples are lower than values achieved in the BSSO thin films [29] and single crystals [20, 27]. The highest charge carrier density of 1.65×10^{21} cm^{-3} and electron mobility of 1.75 cm^2/Vs were found in the $BaSn_{1-x}Sb_xO_3$ thin film with x = 0.07 obtained by pulsed laser deposition (PLD) [29]. On the other hand, the charge carrier density and electron mobility of $BaSn_{1-x}Sb_xO_3$ (x = 0.03) single crystals obtained by molten flux [20, 27], reached 1.02×10^{20} cm^{-3} and 79.4 cm^2/Vs, respectively.

Table 6.

3.4. UV-Vis spectroscopy

UV-Vis Diffuse Reflectance Spectra of $BaSn_{1-x}Sb_xO_3$ pulverized ceramic samples are shown in Figure 12 as a Tauc plot, which presents a modified Kubelka-Munk function $[F(R)h\nu]^{1/2}$, versus photon energy $h\nu$. (Kubelka-Munk function is given by $F(R) = (1–R)^{1/2}/2R$, where R represents measured reflectance relative to a standard [48, 49]). For each

Journal Pre-proof

sample E_g value was obtained as the point of intersection of the tangent line on Tauc plot and the horizontal axis.

Based on literature data BSO has a clear absorption edge at approximately 400 nm, corresponding to the band gap of 3.1 eV [2]. In our case, the undoped sample showed the absorption edge at lower energy and the band gap was 2.92 eV, which is in accordance with some previously reported results [28, 50]. DRS of doped $BaSn_{1-x}Sb_xO_3$ samples showed a reduction of slope, revealing that their absorption edge is moved to larger energies in comparison with BSO. This phenomenon known as a blue shift, or Burstein–Moss effect is noted in some other n-type doped $BaSnO_3$-based materials [2, 14, 27, 51]. Upon doping with Sb, the number of electrons filling the lower energy levels in the conduction band (CB) of BSO is increased, and more energy is needed for the electron transfer from the valence band (VB) to the higher unoccupied energy states in the CB [51]. As a result of this change in electronic states, the Fermi level energy (E_F) moves to the higher energy values [51]. But, for the $BaSn_{0.9}Sb_{0.1}SbO_3$ sample the Fermi level is shifted to the lower energies in comparison with the $BaSn_{0.92}Sb_{0.08}SbO_3$. Doping with the highest Sb concentration led to the formation of electrically inactive Sb, which behave like electron traps for the carriers showing a decrease in carrier density [29]. Furthermore, the created scattering centre originating from electrically inactive Sb can block the electron transport to the conduction band (CB) [29], which results in the decrease of electron mobility. This caused a decrease in the electrical conductivity of $BaSn_{0.9}Sb_{0.1}O_3$ ceramic sample and the loss of linearity in its *I-U* characteristic.

In our samples, as the Hall measurements confirmed, Sb-doping increased the carrier concentration and mobility of the charge carriers, which resulted in the band gap widening. The transparency of visible light for the undoped BSO sample was approximately 80 %, but doping with Sb resulted in a loss of transparency to the visible irradiation. We could conclude

Journal Pre-proof

that presented doped $BaSn_{1-x}Sb_xO_3$ can't find application as a transparent conducting oxide. However, Sb-doping increased the electrical conductivity of $BaSn_{1-x}Sb_xO_3$ samples, and it led to the linearity of *I-U* characteristic, making the $BaSn_{1-x}Sb_xO_3$ samples good candidates for linear resistors.

Fig. 12.

4. Conclusions

Spark plasma sintering method enabled the preparation of Sb-doped barium stannate ceramics in shorter times and at lower temperatures in comparison with the conventional sintering processes. Well densified polycrystalline samples of $BaSn_{1-x}Sb_xO_3$ (x = 0.00, 0.04, 0.06, 0.08 and 0.10) show homogeneous microstructure with reduction of the grain size with the increase of Sb concentration.

Sb-doping of SPS $BaSnO_3$ proved to be useful for tailoring the presence of potential barrier at grain boundaries in ceramic materials. Samples with lower dopant concentration exhibited non-linear *I-U* characteristic typical for semiconductors having potential barriers at grain boundaries. On the other hand, $BaSn_{0.92}Sb_{0.08}O_3$ sample (x = 0.08) showed linear *I-U* characteristic in the whole temperature measurement range and significant drop in the electrical resistivity due to the loss of potential barriers at grain boundaries as a consequence of LAGBs present in this ceramic sample.

Sb-doping also increased n-type carrier concentration and charge carriers mobility in the ceramic samples, resulting in the increase of their electrical conductivity, especially for the $BaSn_{0.92}Sb_{0.08}O_3$. Doping with Sb increased the band gap values, revealing the Burstein–Moss shift (i.e., blue shift) in all doped samples. Hence, $BaSn_{0.92}Sb_{0.08}O_3$ ceramic sample can be used as a linear resistor owing to its appropriate microstructural, electrical and optical properties.

Journal Pre-proof

Journal Pre-proof

Declaration of interests

The authors declare that they have no known competing financial interests or personal relationships that could have appeared to influence the work reported in this paper.

Acknowledgment

The authors acknowledge financial support of Ministry of Education, Science, and Technological Development of Republic of Serbia (Contract No. 451-03-68/2020-14/200053). S. Bernik, M. Podlogar and M. Kocen acknowledge support of Slovenian Research Agency (Program Contract No. P2-0084). The TEM work was conducted in the infrastructure of Centre for Electron Microscopy and Microanalysis (CEMM) in Jožef Stefan Institute, Ljubljana, Slovenia. Ž. Rapljenović and T. Ivek acknowledge the support of Croatian Science Foundation project IP-2018-01-2730. This work was done as a part of the project entitled "Zero-to Three-Dimensional Nanostructures for Application in Optics, Electronics and Energetics" under the bilateral collaboration between Institute for Multidisciplinary Research (University of Belgrade, Serbia) and Institute "Jožef Stefan" (Ljubljana, Slovenia).

References

[1] R. K. Pandey, Fundamentals of electroceramics: materials, devices, and applications, first ed., John Wiley & Sons, Inc., New Jersey, 2019.

[2] H. Mizoguchi, P. Chen, P. Boolchand, V. Ksenofontov, K. Felser, P. W. Barnes, P. M. Woodward, Electrical and Optical Properties of Sb-Doped $BaSnO_3$, Chem. Mater. 25 (19) (2013) 3858-3866.

Journal Pre-proof

Journal Pre-proof

[3] M. A. Peña, J. L. G. Fierro, Chemical Structures and Performance of Perovskite Oxides, Chem. Rev. 101 (2001) 1981-2017.

[4] W. Lu, S. Jiang, D. Zhou, S. Gong, Structural and electrical properties of $Ba(Sn,Sb)O_3$ electroceramics materials, Sens. Actuators 80 (2000) 35-37.

[5] Y. H. O. Muñoz, M. Ponce, J. E. R. Páez, Comparative study of two wet chemical methods of $BaSnO_3$ synthesis: Mechanism of formation of mixed oxide, Powder Technol. 279 (2015) 86-95.

[6] A. M. Azad, N. C. Hon, Characterization of $BaSnO_3$-based ceramics Part 1. Synthesis, processing and microstructural development, J. Alloys Compd. 270 (1998) 95-106.

[7] J. Cerdà, J. Arbiol, G. Dezanneau, R. Díaz, J. R. Morante, Perovskite-type $BaSnO_3$ powders for high temperature gas sensor applications, Sens. Actuators B 84 (2002) 21-25.

[8] M. Yasukawa, T. Kono, K. Ueda, H. Yanagi, S. W. Kim, H. Hosono, Thermoelectric properties and figure of merit of perovskite-type $Ba_{1-x}La_xSnO_3$ with x = 0.002–0.008, Solid State Commun. 172 (2013) 49-53.

[9] A. M. Azad, L. L. W. Shyan, T. Y. Pang, C. H. Nee, Microstructural evolution in $MSnO_3$ ceramics derived via self-heat-sustained (SHS) reaction technique, Ceram. Int. 26 (2000) 685-692.

[10] H. Mizoguchi, H. W. Eng, P. M. Woodward, Probing the Electronic Structures of Ternary Perovskite and Pyrochlore Oxides Containing Sn^{4+}or Sb^{5+}, Inorg. Chem. 43 (2004) 1667-1680.

[11] C. Moure, Octavio Peña, Recent advances in perovskites: Processing and properties, Prog. Solid State Chem. 43 (2015) 123-148.

[12] David O. Scanlon, Defect engineering of $BaSnO_3$ for high-performance transparent conducting oxide applications, Phys. Rev. B 87 (2013) 161201(R).

Journal Pre-proof

Journal Pre-proof

[13] U. Kumar, Md. J. Ansaree, S. Upadhyay, Structural and optical characterizations of $BaSnO_3$ nanopowder synthesized by aqueous sol-gel method, Process. Appl. Ceram. 11 (3) (2017) 177-184.

[14] A. Slassi, Ab initio study of a cubic perovskite: Structural, electronic, optical and electrical properties of native, lanthanum- and antimony-doped barium tin oxide, Mat. Sci. Semicon. Proc. 32 (2015) 100-106.

[15] C. Huang, X. Wang, X. Liu, M. Tian, T. Zhang, Extensive analysis of the formation mechanism of $BaSnO_3$ by solid-state reaction between $BaCO_3$ and SnO_2, J. Eur. Ceram. Soc. 36 (2016) 583-592.

[16] M. Bilal Saddique, M. Rashid, A. Afzal, S. M. Ramay, F. Aziz, A. Mahmood, Ground state opto-electronic and thermoelectric response of cubic $XSnO_3$ (X = Ba, Sr) compounds, Curr. Appl. Phys. 17 (2017) 1079-1086.

[17] P. Udawatte, M. Kakihana, M. Yoshimura, Preparation of pure perovskite-type $BaSnO_3$ powders by the polymerized complex method at reduced temperature, Solid State Ion. 108 (1998) 23-30.

[18] G. Wang, J. Bai, C. Shan, D. Zhang, N. Lu, Q. Liu, Z. Zhou, S. Wang, C. Liu, Synthesis and ethanol gas sensing properties of mesoporous perovskite type $BaSnO_3$ nanoparticles interconnected network, Mater. Lett. 205 (2017) 169-172.

[19] I. A. Alagdal, A. R. West, Oxygen stoichiometry, conductivity and gas sensing properties of $BaSnO_3$, J. Mater. Chem. C 4 (2016) 4770-4777.

[20] W.-J. Lee,H. J. Kim, J. Kang, D. H. Jang, T. H. Kim, J. H. Lee, K. H. Kim, Transparent Perovskite Barium Stannate with High Electron Mobility and Thermal Stability, Annu. Rev. Mater. Res. 47 (2017) 391-423.

[21] M. G. Smith, J. B. Goodenough, A. Manthiram, Tin and Antimony Valence States in $BaSn_{0.85}Sb_{0.15}O_{3-\delta}$, J. Solid State Chem. 98 (1992) 181-186.

Journal Pre-proof

Journal Pre-proof

[22] R. J. Cava, P. Gammel, B. Batlogg, J. J. Krajewski, W. F. Peck, Jr., L. W. Rupp, Jr., R. Felder, R. B. van Dover, Nonsuperconducting $BaSn_{1-x}Sb_x O_3$. The 5s-orbital analog of $BaPb_{1-x}Bi_xO_3$, Phys. Rev. B. 42 (7) (1990) 4815-4818.

[23] M. G. Smith, J .B. Goodenough, Electronic structure of $BaSn_{1-x}Sb_xO_3$ studied by photoemission spectroscopy, Phys. Rev. B. 47 (4) (1993) 1788-1793.

[24] T. Huang, T. Nakamura, M. Itoh, Y. Inaguma, O. Ishiyama, Electrical properties of $BaSnO_3$ in substitution of antimony for tin and lanthanum for barium, J. Mater. Sci. 30 (1995) 1556-1560.

[25] G. Pfaff, Wet Chemical Powders Synthesis of $BaSnO_3$ and Ba_2SnO_4, J. Eur. Ceram. Soc. 12 (1993) 159-164.

[26] D. Yamashita, S. Takefuji, M. Tsubomoto, T. Yamamoto, Electronic structure analysis of Sb-doped $BaSnO_3$, Mat. Sci. Eng. B 173 (2010) 33-36.

[27] H. J. Kim, J. Kim, T. H. Kim, W.-J. Lee, B.-Gu Jeon, J.-Y. Park, W. S. Choi, D. W. Jeong, S. H. Lee, J. Yu, T. W. Noh, K. H. Kim, Indications of strong neutral impurity scattering in $Ba(Sn,Sb)O_3$ single crystals, Phys. Rev. B 88 (2013) 125204.

[28] Z. Galazka, R. Uecker, K. Irmscher, D. Klimm, R. Bertram, A. Kwasniewski, M. Naumann, R. Schewski, M. Pietsch, U. Juda, A. Fiedler, M. Albrecht, S. Ganschow, T. Markurt, C. Guguschev, M. Bickermann, Melt growth and properties of bulk $BaSnO_3$ single crystals, J. Phys.: Condens. Matter 29 (2017) 075701.

[29] Q. Liu, J. Dai, Z. Liu, X. Zhang, G. Zhu, G. Ding, Electrical and optical properties of Sb-doped $BaSnO_3$ epitaxial films grown by pulsed laser deposition, J. Phys. D: Appl. Phys. 43 (2010) 455401

[30] R. Wei, X. Tang , L. Hu, X. Luo, J. Yang, W. Song, J. Dai, X. Zhu, Y. Sun, Growth, Microstructures, and Optoelectronic Properties of Epitaxial $BaSn_{1-x}Sb_xO_{3-\delta}$ Thin Films by Chemical Solution Deposition, ACS Appl. Energy Mater. 1 (4) (2018)1585-1593.

Journal Pre-proof

Journal Pre-proof

[31] S. Raghavan, T. Schumann, H. Kim, J. Y. Zhang, T. A. Cain, S. Stemmer, High-mobility $BaSnO_3$ grown by oxide molecular beam epitaxy, APL Mater. 4 (2016) 016106.

[32] A. Prakash, J. Dewey, H. Yun, J. S. Jeong, K. A. Mkhoyan, B. Jalan, Hybrid molecular beam epitaxy for the growth of stoichiometric $BaSnO_3$, J Vac Sci Techol A 33 (2015) 060608.

[33] Y. Z. Wang, E. Bevillon, A. Chesnaud, G. Geneste, G. Dezanneau, Atomistic Simulation of Pure and Doped $BaSnO_3$, J. Phys. Chem. C 113 (2009) 20486-20492.

[34] S. Liu, W. Ding, Y. Gu, W. Chai, Effect of Sb doping on the microstructure and optoelectrical properties of Sb-doped SnO_2 films prepared by spin coating, Phys. Scripta 85 (2012) 065601.

[35] Y. Li, L. Zhang, Y. Ma, D. J. Singh, Tuning optical properties of transparent conducting barium stannate by dimensional reduction, APL Materials 3 (2015) 011102.

[36] Z. Branković, D. Lukovic Golić, A. Radojković, J. Ćirković, D. Pajić, Z. Marinković Stanojević, J. Xing, M. Radović, G. Li, G. Branković, Spark plasma sintering of hydrothermally synthesized bismuth ferrite, Process. Appl. Ceram. 10 (4) (2016) 257-264.

[37] R. Licheri, S. Fadda, R. Orrù, G. Cao, V. Buscaglia, Self-propagating high-temperature synthesis of barium titanate and subsequent densification by spark plasma sintering (SPS), J. Eur. Ceram. Soc. 27 (2007) 2245-2253.

[38] N. Okinaka, L. Zhang, T. Akiyama, Thermoelectric Properties of Rare Earth-doped $SrTiO_3$ Using Combination of Combustion Synthesis (CS) and Spark Plasma Sintering (SPS), ISIJ International 50 (9) (2010) 1300-1304.

[39] R.G. Garwey, Computer Comments, Powder Diffract. 1 (1986) 114-118.

[40] F. Delorme, R. Dujardin, F. Schoenstein, B. Pintault, P. Belleville, C. Autret, I. Monot-Laffez, F. Giovannelli, Nanostructuring of dense SnO_2 ceramics by Spark Plasma Sintering, Ceram. Int. 45 (2019) 8313-8318.

Journal Pre-proof

[41] H. Yoshida, K. Morita, B.-N. Kim, K. Soga, Low temperature spark plasma sintering of tin oxide doped with tantalum oxide, J. Ceram. Soc. Jpn 124 (9 (2016) 932-937.

[42] B. Hadjarab, A. Bouguelia, M. Trari, Optical and transport properties of lanthanum-doped stannate $BaSnO_3$, J. Phys. D: Appl. Phys. (40) (2007) 5833-5839.

[43] J. Wu, F. Chen, Q. Shen, J. M. Schoenung, L. Zhang, Spark Plasma Sintering and Densification Mechanisms of Antimony-Doped Tin Oxide Nanoceramics, J. Nanomater. (2013) ID 561895 (7 pages).

[44] WebElements^{TM}, The periodic table of the elements, https://www.webelements.com/.

[45] Y. Furushima, A. Nakamura, E. Tochigi, Y. Ikuhara, K. Toyoura, K. Matsunaga, Dislocation structures and electrical conduction properties of low angle tilt grain boundaries in $LiNbO_3$, J. Appl. Phys. 120 (2016) 142107 1-10.

[46] H. Li, G. Zhao, X. Zeng, G. Zhou, Z. Qian, S. Zhou, J. Xu, Study on cracking and low-angle grain boundary defects in $YAlO_3$ crystal, Mater. Lett. 58 (2004) 3253-3256.

[47] C. Wang, K. Du, K. Song, X. Ye, L. Qi, S. He, D. Tang, N. Lu, H. Jin, F. Li, H. Ye, Size-Dependent Grain-Boundary Structure with Improved Conductive and Mechanical Stabilities in Sub-10-nm Gold Crystals, Phys. Rev. Lett.120 (2018) 186102.

[48] P. Kubelka, F. Munk, An Article on Optics of Paint Layers, Z. Tech. Phys. 12 (1931) 593.

[49] J. Tauc, R. Grigorovici, A. Vancu, Optical Properties and Electronic Structure of Amorphous Germanium, Phys. Status Solidi 15 (1966) 627-637.

[50] R. Kurre, S. Bajpai, P. Kumar Bajpai, Synthesis, Characterization, Optical and Transport Properties of $BaSnO_3$ Synthesized by Wet Chemical Route, J. Mater. Sci. 9 (2018) 92-110.

[51] A. Sarkar, S. K. De, Defect and Optical Properties of Sb doped and hydrogenated $BaSnO_3$, Semicond. Sci. Technol. 33 (2018) 035018.

Journal Pre-proof

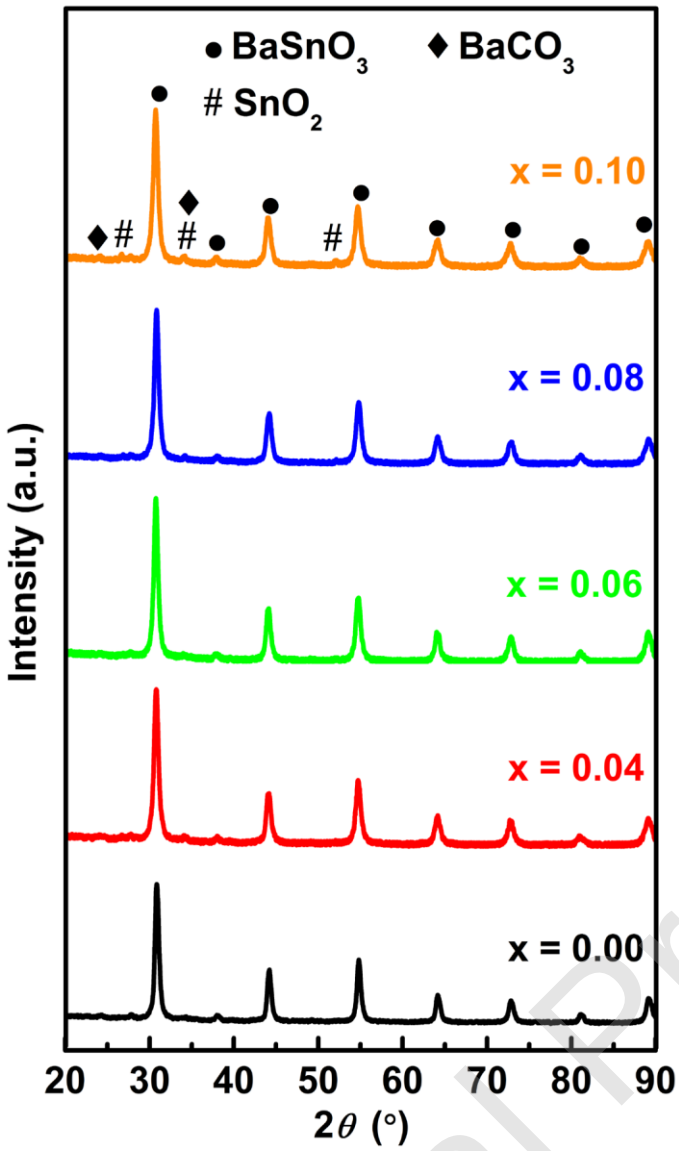

Figure 1. XRD patterns of $BaSn_{1-x}Sb_xO_3$ powders calcined at 900 °C for 4 h in air.

Journal Pre-proof

Journal Pre-proof

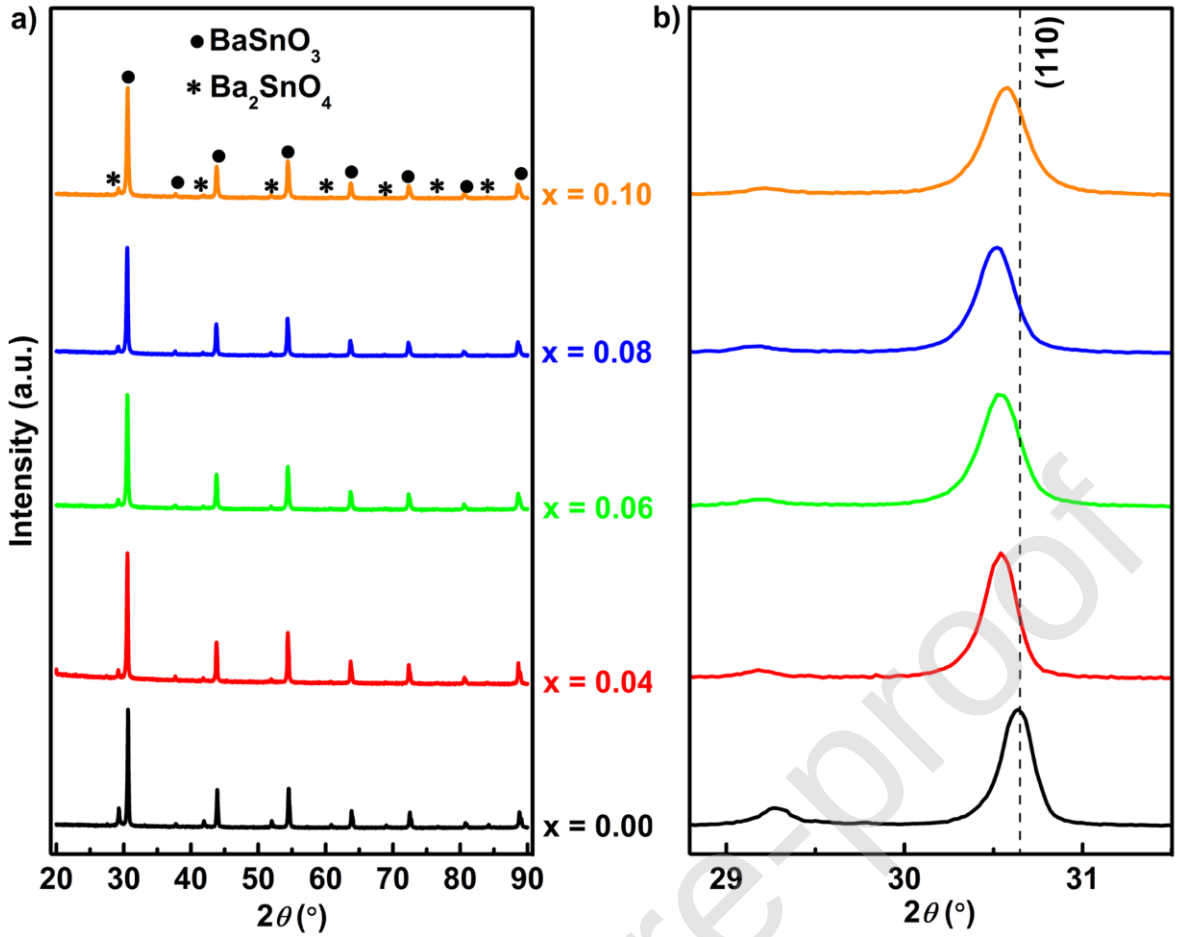

Figure 2. (a) XRD patterns of the pulverized $BaSn_{1-x}Sb_xO_3$ ceramic samples after the SPS treatment; (b) Shifting of the strongest (110) reflection of $BaSn_{1-x}Sb_xO_3$ ceramic samples.

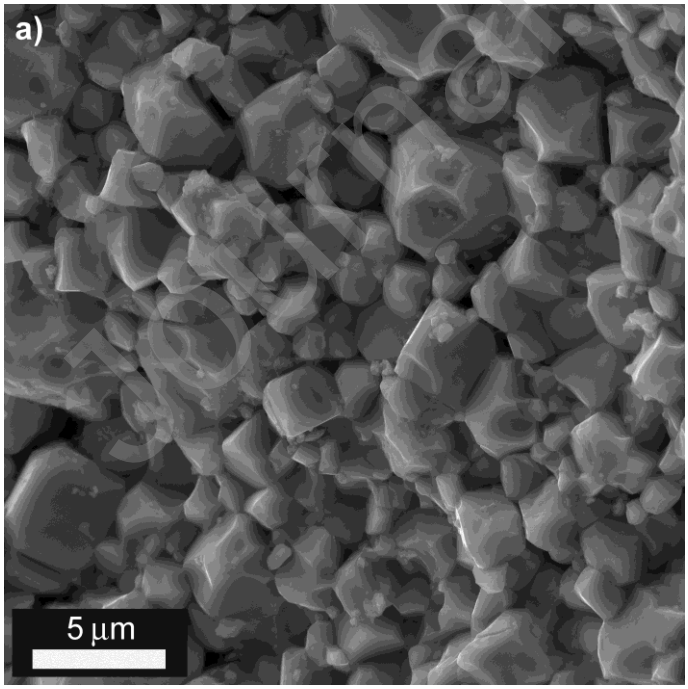

Journal Pre-proof

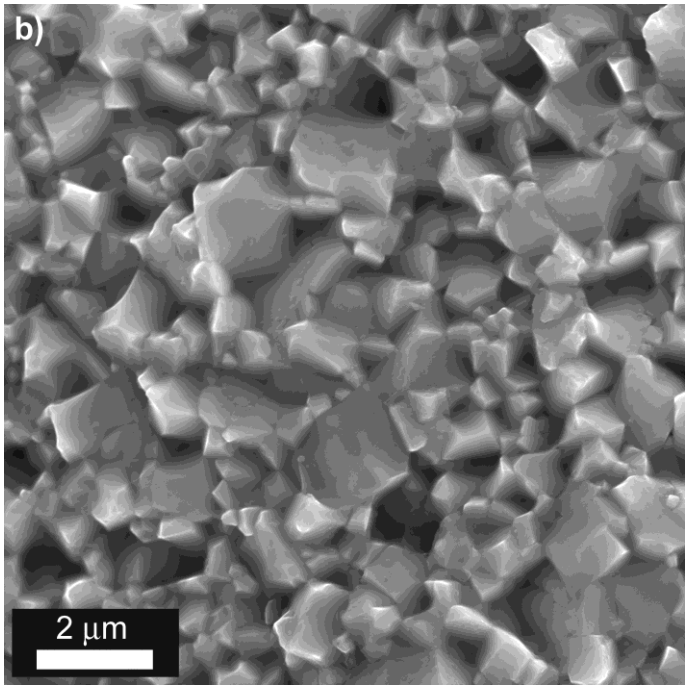

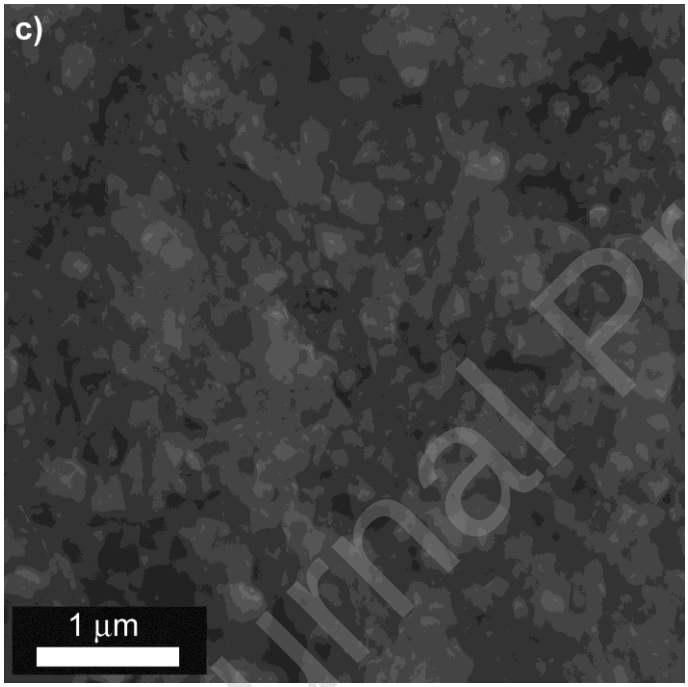

Journal Pre-proof

Journal Pre-proof

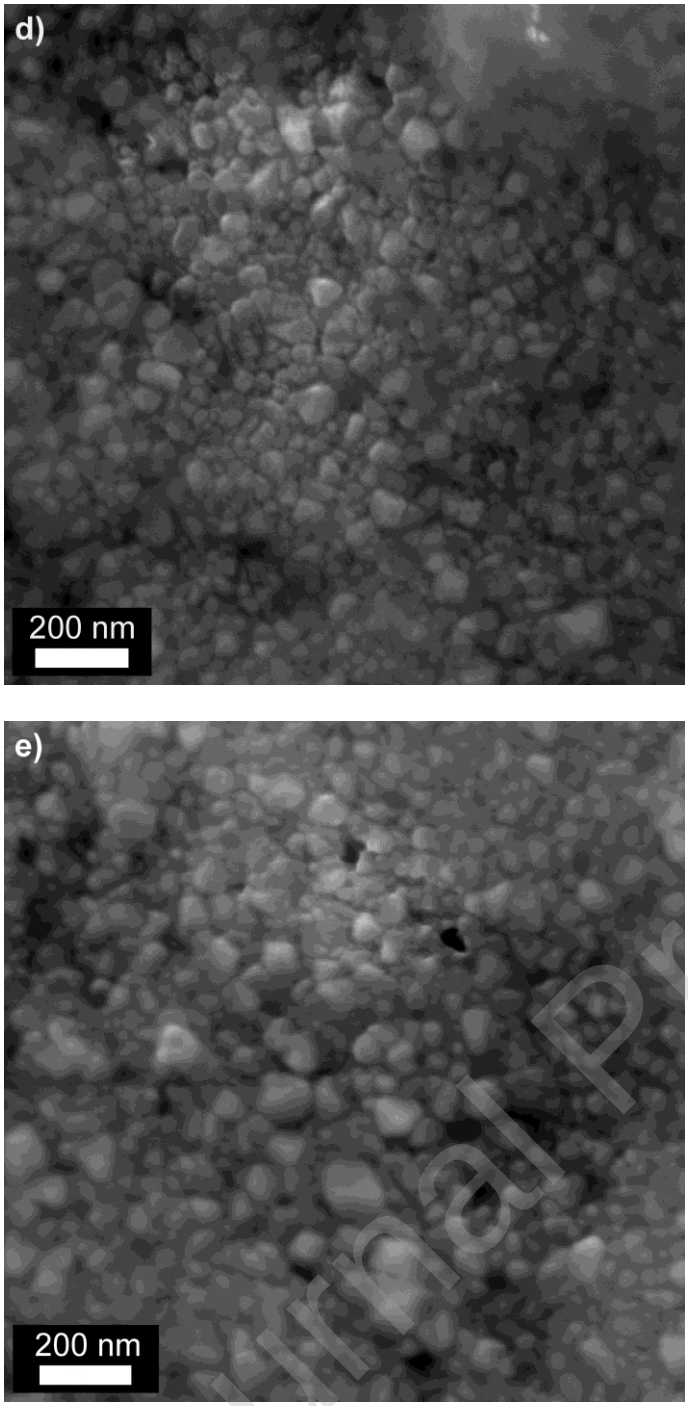

Figure 3. FESEM micrographs of the fractured cross-sections of $BaSn_{1-x}Sb_xO_3$ ceramic samples: (a) x = 0.00, (b) x = 0.04, (c) x = 0.06, (d) x = 0.08 and (e) x = 0.10.

Journal Pre-proof

Journal Pre-proof

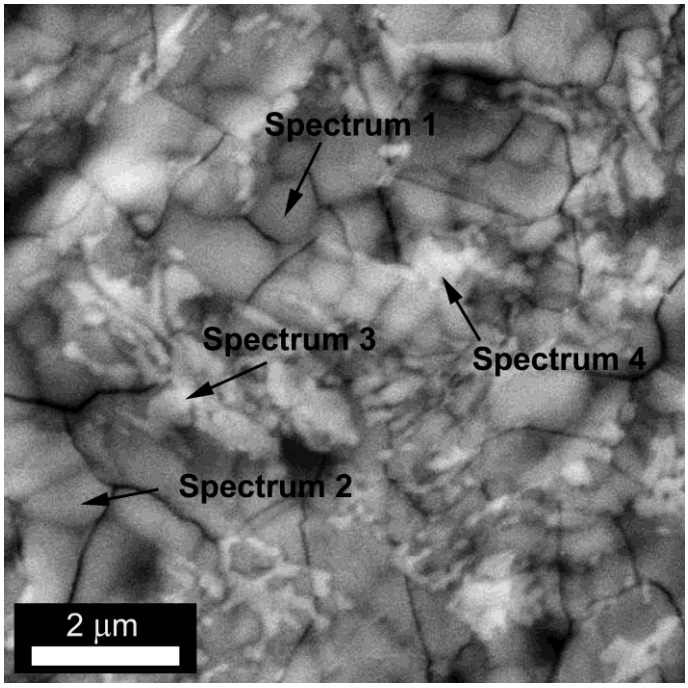

Figure 4. BS-SEM micrograph of the undoped BSO ceramic sample's polished surface thermally etched at 1100 °C/20 min.

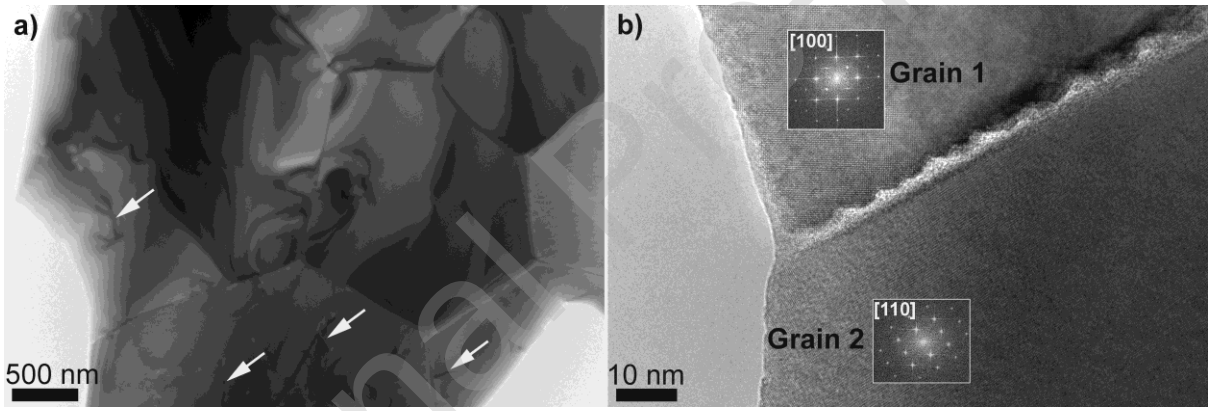

Figure 5. (a) TEM micrograph of the undoped $BaSnO_3$ pellet with marked dislocations (b) HRTEM micrograph of the undoped $BaSnO_3$ pellet (The insets present the fast Fourier transform (FFT) of micrographs of both grains tilted into zone axis).

Journal Pre-proof

Journal Pre-proof

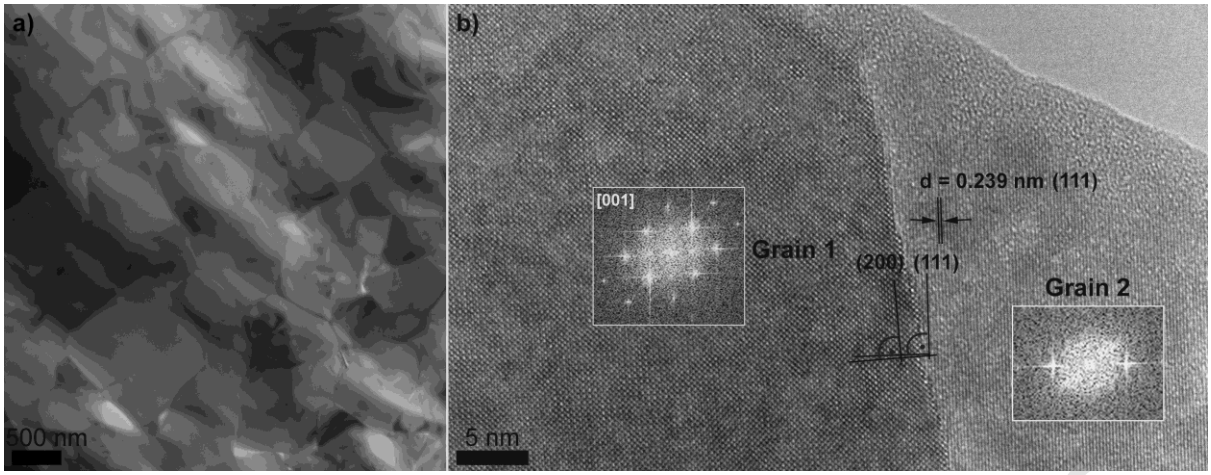

Figure 6. (a) TEM micrograph of the $BaSn_{0.96}Sb_{0.04}O_3$ pellet, (b) HRTEM micrograph of the $BaSn_{0.96}Sb_{0.04}O_3$ pellet (The insets present FFT, of Grain 1 oriented along [001] direction and Grain 2 out of zone axis).

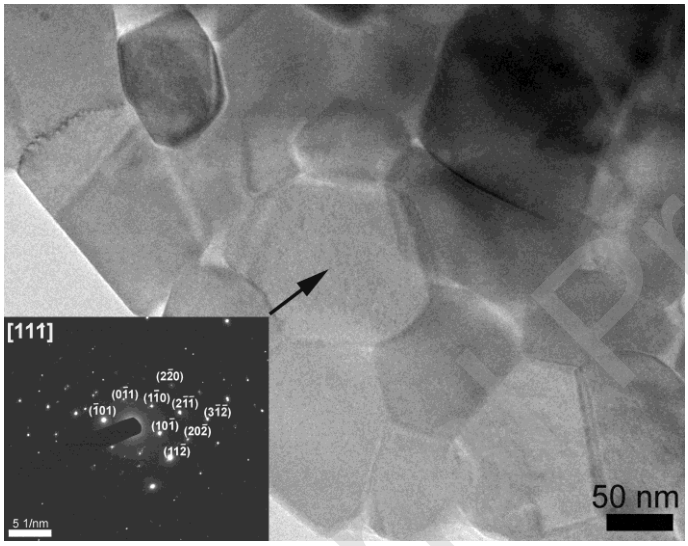

Figure 7. TEM micrograph of $BaSn_{0.92}Sb_{0.08}O_3$ sample. The inset shows SAED pattern of grain oriented along [111] direction.

Journal Pre-proof

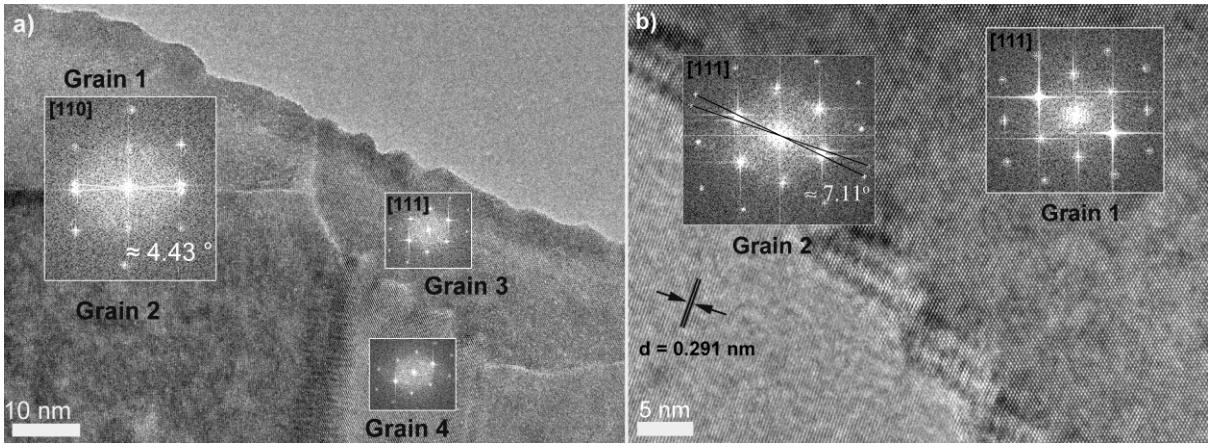

Figure 8. HRTEM micrographs of the $BaSn_{0.92}Sb_{0.08}O_3$ ceramic sample showing LAGB formed between pairs of grains oriented along: (a) [110] and [111] direction; (b) [111] direction. (The insets present FFT of grains micrographs).

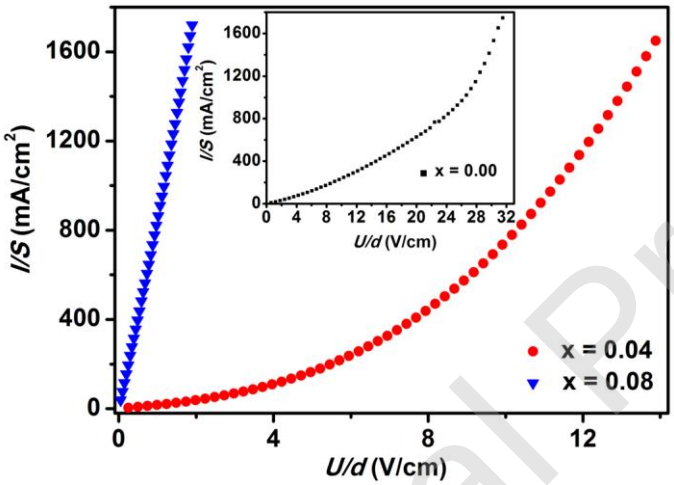

Figure 9. *I-U* characteristic of $BaSn_{1-x}Sb_xO_3$ (x = 0.04 and 0.08) ceramic samples measured in air at 25 ºC. Inset: *I-U* characteristic of undoped BSO ceramic sample measured under the same conditions.

Journal Pre-proof

Journal Pre-proof

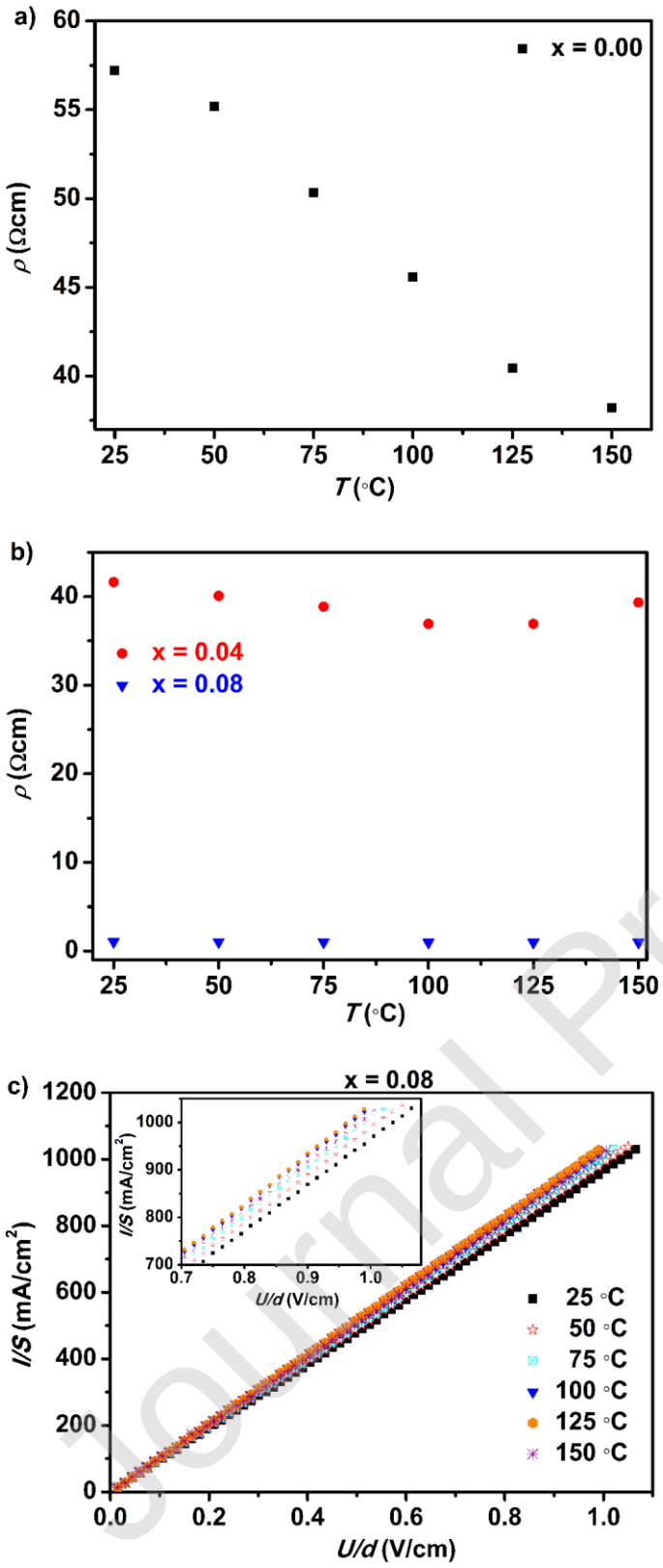

Figure 10. Electrical resistivity as a function of temperature for $BaSn_{1-x}Sb_xO_3$ samples: (a) x = 0.00; (b) x = 0.04 and 0.08. (c) I-U characteristic of $BaSn_{0.92}Sb_{0.08}O_3$ sample, measured in

Journal Pre-proof

the temperature range (25–150) °C. Inset graph: *I-U* characteristic of $BaSn_{0.92}Sb_{0.08}O_3$ sample in the range of (0.7-1.1) V/cm.

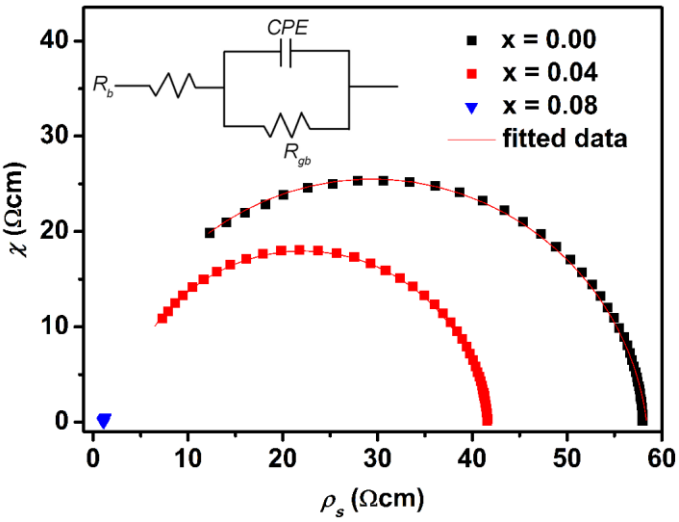

Figure 11. AC impedance data fitted to the circuit (shown as the inset) for the x = 0.00, 0.04 and 0.08 samples measured at 25 °C.

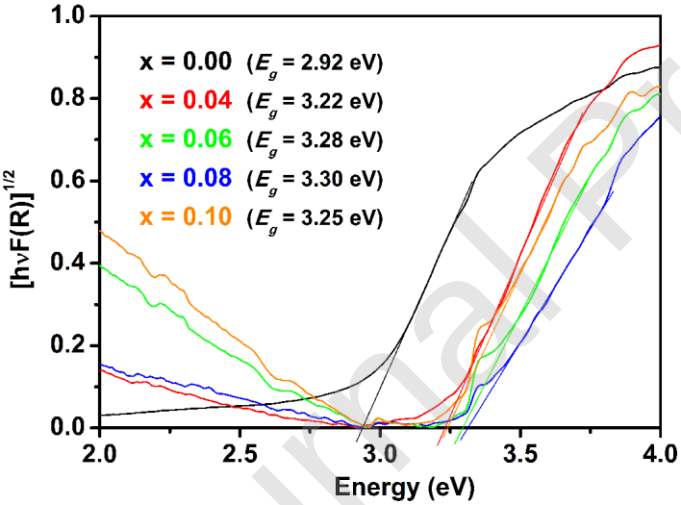

Figure 12. Tauc plots of pulverized $BaSn_{1-x}Sb_xO_3$ (x = 0.00 – 0.10) ceramic samples.

Table 1. The phase content of cubic $BaSnO_3$ phase, unit cell parameter (a), average crystallite size, grain size, and relative density for $BaSn_{1-x}Sb_xO_3$ ceramic samples.

$BaSn_{1-x}Sb_xO_3$	$BaSnO_3$ phase content [wt %]	Unit cell parameter, a [Å]	Crystallite size [nm]	Grain size [nm]	Rel. density [%TD*]
x = 0.00	85.00	4.1227(4)	57	1500	96
x = 0.04	93.10	4.1287(9)	49	650	95
x = 0.06	92.38	4.1301(9)	39	112	84

Journal Pre-proof

Journal Pre-proof

x = 0.08	92.21	4.1321(9)	43	44	86
x = 0.10	92.11	4.1302(4)	37	53	79

*TD: theoretical density

Table 2. The comparison of theoretical and ICP experimental molar ratios of Ba, Sn and Sb in annealed ceramic $BaSn_{1-x}Sb_xO_3$ samples.

$BaSn_{1-x}Sb_xO_3$	**Ba : Sn : Sb molar ratio theor.**	**Ba : Sn : Sb molar ratio ICP**
x = 0.00	1 : 1 : 0	1 : 0.79 : 0
x = 0.04	1 : 0.96 : 0.04	1 : 0.75 : 0.036
x = 0.08	1 : 0.92 : 0.08	1 : 0.72 : 0.08

Table 3. EDS analysis of undoped BSO sample.

Spectra	**Atomic % of elements**		
	Ba	**Sn**	**O**
Spectrum 1	20.35	20.74	58.91
Spectrum 2	19.17	19.85	60.98
Spectrum 3	19.72	15.51	64.77
Spectrum 4	20.17	17.24	62.59

Table 4. The dependence of DC electrical resistivity on the antimony concentration for $BaSn_{1-x}Sb_xO_3$ ceramic samples.

$BaSn_{1-x}Sb_xO_3$	**x = 0.00**	**x = 0.04**	**x = 0.08**
DC electrical resistivity [Ωcm]	56.81	41.27	1.09

Table 5. The calculated values for bulk resistivity (ρ_b), grain boundary resistivity (ρ_{gb}), capacitance (P), coefficient of constant phase element (p) and total electrical resistivity (ρ) for $BaSn_{1-x}Sb_xO_3$ ceramic samples.

$BaSn_{1-x}Sb_xO_3$	**Bulk resistivity ρ_b [Ωcm]**	**Grain boundary resistivity ρ_{gb} [Ωcm]**	**Capacitance P [nF]**	**Coefficient of CPE CPE-p**	**Total electrical resistivity ρ[Ωcm]**
x = 0.00	5.1	52.79	1.4372	0.92	57.89
x = 0.04	2.77	38.89	2.8681	0.95	41.66

Journal Pre-proof

Journal Pre-proof

***x* = 0.08**	-	-	-	-	1.12

Table 6. The values of electrical bulk resistivity, Hall coefficient, charge carrier density and mobility for $BaSn_{1-x}Sb_xO_3$ ceramic samples. (Charge carrier concentration and carrier mobility are shown in a single-carrier-type picture). For comparison, corresponding values for thin films [29] and single crystals [20, 27] are included in the Table.

	Ceramic materials			**Thin films [29]**	**Single crystals [20, 27]**
Sb-content, *x* [mol]	**0.00**	**0.04**	**0.08**	**0.07**	**0.03**
Electrical bulk resistivity, ρ_b [Ωcm]	5.10	2.77	1.12	2.43×10^{-3}	0.66×10^{-3}
Hall coefficient [cm^3/C]	-0.8±0.1	-0.64±0.02	-0.33±0.02	-	-
Carrier density [$\times10^{18}$ cm^{-3}]	8±1	9.7±0.3	19±1	1.65×10^{3}	102
Carrier mobility [cm^2/Vs]	0.16±0.02	0.231±0.007	0.29±0.02	1.75	79.4

Journal Pre-proof